Electrical and morphological behavior of carbon nanotubes synthesized within porous anodic alumina templates

Leandro Sacco, Ileana Florea, Marc Châtelet, Costel-Sorin Cojocaru

Electrical and morphological behavior of carbon nanotubes synthesized within porous anodic alumina templates

JPhys Materials

PAPER

Electrical and morphological behavior of carbon nanotubes synthesized within porous anodic alumina templates

Leandro Sacco[1], **Ileana Florea, Marc Châtelet and Costel-Sorin Cojocaru**

Laboratoire de Physique des Interfaces et des Couches Minces (LPICM), CNRS, Ecole Polytechnique, Université Paris Saclay, 91128, Palaiseau Cedex, France

[1] Author to whom any correspondence should be addressed.

E-mail: leandro.sacco@polytechnique.edu

Keywords: carbon nanotubes, porous anodic alumina, barrier thinning layer, branched structures, electrodeposition

Supplementary material for this article is available online

OPEN ACCESS

RECEIVED
25 May 2018

REVISED
17 July 2018

ACCEPTED FOR PUBLICATION
24 July 2018

PUBLISHED
17 September 2018

Abstract

The synthesis of carbon nanotubes (CNTs) within porous anodic alumina (PAA) templates requires better understanding regarding their dynamic growth evolution, and how this is influenced by the geometrical features of the PAA. The growth of nanostructures, such as CNTs, becomes more complex when an exponential voltage decrease process is applied to thin the dielectric layer of the PAA matrix, because this process leads to the formation of a branched structure at the bottom of the pores. Here, we present direct evidence of the impact of the branched structure at the bottom of the PAA at different time-stages of the CNT synthesis. These studies reveal that when numerous branches are created, competition between the growing nanotubes is established during their formation. Additionally, large pores lead to flattened catalyst electrodeposition, promoting tube entanglement since more than one tube can grow in each pore. Interestingly, two different electrical behaviors are measured when considering PAA/CNT devices: linear response in the case of CNTs connecting two parallel electrodes, and nonlinear when junctions between the tubes are being promoted. These results highlight the relevance of having an in-depth understanding of the CVD growth evolution of carbon nanostructures within PAA templates, and simultaneously serve as a guiding procedure towards the fabrication of devices based on parallel organized CNT arrays.

1. Introduction

Carbon nanotubes (CNTs) have been widely used in various applications due to their exceptional thermal [1], mechanical [2], electronic [3] and optoelectronic [4] properties and their remarkable chemical stability [5]. However, several applications, such as energy storage [6], field emitters [7] and composites [8, 9] among others [10–12], require strict control of the CNT size, location and orientation. The confined synthesis of CNTs within porous anodic alumina (PAA) templates appears to be an attractive solution to address the problem of collective self-organized growth, considering that PAA templates offer a wide range of pore sizes and distribution patterns that can be easily obtained by varying the anodization parameters [13, 14].

Carbon nanostructure growth inside porous templates can be performed using two different approaches. The first one consists of the deposition of an amorphous structure on the internal pore walls by the high-temperature pyrolysis of a carbon feedstock [15]. However, such a procedure leads to carbon nanostructures characterized by poor crystallinity, and the tube growth is limited by the pore length. The second approach uses CNT growth by chemical vapor deposition (CVD) methods on metal nanoparticles (NPs) pre-deposited, for example, by an electrodeposition process at the bottom of the pores [16, 17]. In this case, the resulting nanostructures present a significantly higher crystalline quality, which is a desirable characteristic for electronic applications.

The two-step anodization process [18] is the simplest and cheapest method for PAA template fabrication. However, such methods lead to the formation of an oxide barrier layer at the bottom of the pores, which

constitutes an important limitation for subsequent electrodeposition implementation. In order to successfully perform metal-catalyst electrodeposition and overcome the drawbacks related to the oxide barrier layer of the bottom pore [19–22], preliminary procedures/steps have to be introduced before CNT growth. In the present work, an exponential decrease of the anodization voltage at the end of the second step of the anodization process [23, 24] is applied followed by a wet chemical etching procedure. This appears to be a very effective procedure to thin the barrier layer at the bottom of the pores and avoid its expansion. Nevertheless, the exponential voltage decrease process also leads to the creation of a branched structure at the bottom of the pores, which can impact the subsequent synthesis of the nanostructures [25].

Despite the fact that various applications based on CNT arrays synthesized within PAA templates have been developed [17, 26–29], it is worth pointing out that many reports have mainly focused on carbon nanostructure synthesis [30–33] rather than the impact of the porous template features on the synthesized CNT. For instance, Sui *et al* [34] studied the structural and thermal stability as well as the deformation of CNTs inside PAA templates, with and without the utilization of a catalyst. Additionally, Haase *et al* [35] addressed the templating influence on the CNT by studying the effect of porous alumina support on CNTs grown from various metal thicknesses of the catalyst. In consequence, there is a lack of information concerning the influence of the pore structure on the as-grown CNTs.

The main difficulty for addressing the influence of the template effects lies in the complicated experimental measurement procedure for determining CNT yields, the number of tubes grown per each pore and the CNT characteristics in terms of length, diameter and growth rate. It is complicated to extract such CNT characteristics when a low density of tubes per unit of area is grown [25, 36–38], or when a rather dense, spaghetti-like distribution of CNTs occurs [16, 39, 40]. In an attempt to solve such an inconvenience, Jeong *et al* [41] performed an ultrasonication process in order to cut the part of the tube that emerges from the pores of the PAA. Such a method can produce a high-density CNT array inside the pores, but the applied process can also degrade the structure of the tubes.

In the present work, we synthesised CNTs within PAA templates using the double hot-filament CVD (dHF-CVD) method previously described [42]. In order to achieve the effective thinning of the oxide barrier layer at the bottom of the pores, an exponential voltage decrease process was applied followed by wet chemical etching. Herein, we studied the impact of the pore structure close to the bottom zone, on the resulting CNT distribution in terms of their size and yield, emerging/or not from the template pores. A detailed structural and morphological characterization is obtained by preparing thin lamellas by a focused ion beam (FIB) technique and further TEM/STEM analyses, including chemical mapping, through a spectroscopic technique such as energy dispersive x-ray spectroscopy (EDX) [43, 44]. These studies provide more insight and better understanding of the growth dynamic of carbon nanostructures within the pores, and for the first time the supplementary geometrical features that are added when a branched structure is created at the bottom of the pores are accounted for. Finally, electrical characterizations through *I*–*V* measurements were carried out, by fabricating devices with top metallic electrodes deposited on samples in which the CNT synthesis stops when the tube tips begin to emerge from the top of the nanopores. The different observed electrical behavior correlates to the template structure at the bottom of the pores. Since a metallic top electrode is deposited, the electrical transport behavior is determined by the nature of the synthesized carbon nanostructure and the work function value of the electrode [45, 46]. For instance, multi-walled CNTs with diameters larger than 15 nm present metallic electrical behavior [47]. Therefore, ohmic responses are expected for devices based on CNT arrays grown inside PAA templates, as shown in Rochford *et al* [48]. However, nonlinearities can arise in the case of CNT bundles or forests grown on planar substrates due to the tunneling of charge carriers crossing nanotube junctions [49]. So, different electrical behavior is expected depending on the CNT distribution grown within the PAA, imposed by different pore geometries. In the case of hierarchical templates, nanotube junctions are promoted, leading to nonlinear responses. Under the configuration of a PAA with straight pores, parallel tubes directly connected between the electrodes are mainly obtained, and consequently resistor behavior occurs. The present article aims to set the basis of a controlled fabrication process of future devices based on CNTs grown inside PAA templates, providing a method for growing individual tubes inside the pores or by tailoring the number of branches, intentionally creating CNT-CNT junctions.

2. Experimental

2.1. PAA template preparation and characterization

High-purity aluminum foils (Alfa Aesar 99.99%) were cut into pieces 1 cm × 1 cm in size. The aluminum substrates were first cleaned in acetone followed by isopropanol in an ultrasonic bath for 15 min and subsequently rinsed with deionized water. The aluminum substrates had been electropolished in a solution containing a 1:4 mixture of $HClO_4$:C_2H_5OH at 5 °C temperature for 6 min while applying a 20 V potential. For

Table 1. Pretreatment and synthesis conditions involved in the synthesis of CNTs within PAA templates using the dHF-CVD technique.

Process	Pressure (mbar)	H_2 flow (sccm)	CH_4 flow (sccm)	HF-Power H_2 (W)	HF-Power CH_4 (W)	Temperature (°C)	Duration (s)
Pretreatment	50	100	0	0	0	500	120
Synthesis	50	50	50	180	130	500	45–900

the PAA template fabrication, a two-step anodization process was used in a two-electrode electrochemical cell system. A graphite counter electrode was chosen as the cathode and the polished aluminum foils as an anode. The first anodization step was performed for 2 h in a 0.3 M oxalic acid solution at 17.5 °C. Various anodization potentials were applied in the range 20–60 V in increments of 10 V in order to study the branch formation. For each sample, the resulting PAA layer was removed in a mixture solution of 0.2 M CrO_3 and 0.6 M H_3PO_4 at 60 °C for 2 h in order to create nano-imprints with closely packed hexagonal arrays on the aluminum surface. The second step of the anodization process was carried out under the same conditions as the first step for 8 min. In order to reduce the thickness of the oxide barrier layer, an exponential voltage decay process was applied immediately at the end of the second anodization step. The voltage as a function of time $U(t)$ is expressed in the following equation:

$$U(t) = V_0 \exp^{(-\eta * t)} + V'. \tag{1}$$

The time constant η gives the rate of the voltage decrease. On the other hand V_0 and V' are free parameters whose ideal values will depend on the chosen applied constant voltage during the anodization process. In the present study, for all the studied anodization potentials, the same exponential decay time constant was used, taking as reference a previous work performed by Marquadt *et al* [24], where $\eta = 2 \times 10^{-3} \frac{1}{s}$. Concerning the voltage constants V_0 and V', their values were determined considering the following expressions:

$$V_0 = V_A + 10\ \text{V} \tag{2}$$

$$V' = -10\ \text{V} \tag{3}$$

where V_A is the anodization potential. The final applied anodization potential value was set at 4.97 V. In order to fully remove the oxide barrier layer at the bottom of the pores, the resulting PAA templates were immersed in a wet chemical etching solution of 0.3 M H_3PO_4 at 30 °C for 25 min.

The PAA pore characteristics, such as the pore diameter, interpore distance and regularity of the pores, are shown in the supporting information section following previously reported procedures [50, 51].

2.2. Electrodeposition of the nickel catalyst nanoparticles within the PAA template

Nickel nanoparticles were deposited within the PAA templates via an electrodeposition process using a three-electrode setup, with a Ag/AgCl electrode as a reference electrode, the PAA template itself as a working electrode and a graphite counter electrode. The setup was supplied with a Bio-Logic potentiostat and EC-lab software for setting the electrodeposition parameters and designing the shape of the pulses applied to the working electrode. The electrodeposition process was performed in a Watts bath solution consisting of a mixture of 330 g l^{-1} $NiO_4 \cdot 6H_2O$, 45 g L^{-1} $NiCl_2 \cdot 6H_2O$, and 45 g l^{-1} H_3BO_3. Pulses of 5 ms with a potential amplitude of −5.5 V followed by a 90 ms resting time in an open voltage circuit were applied to electrodeposited Ni NPs. The number of total pulses was set at 50 for all the fabricated samples. A more detailed description of the electrodeposition technique is explained elsewhere [24].

2.3. Synthesis of CNTs within PAA templates

The CNT synthesis within the PAA template was carried out by means of a double-hot-filament-assisted chemical vapor deposition (dHF-CVD) technique using methane (CH_4) as a gas precursor. The dHF-CVD technique enables the local thermal pre-decomposition of the molecules involved in the synthesis prior to reaching the sample with the catalyst nanoparticles. This implementation of the dHF-CVD technique enables the synthesis of CNTs at relatively lower temperatures (500 °C–800 °C) than the conventional thermal CVD process. The set-up characteristics are detailed elsewhere [42]. The PAA/Ni assemblies were placed inside a tubular quartz reactor and thermally treated at 500 °C for 2 min under H_2 flow for the activation of the Ni nanoparticle catalyst. After the activation step, the H_2 flow was further replaced by a mixture of CH_4 /H_2 while the reactor temperature was kept at the same temperature for the whole synthesis process. The pretreatment and synthesis conditions are summarized in table 1. Various synthesis durations from 45 s to 900 s were used in order to determine the moment that the tubes begin to emerge from the pores.

2.4. Device fabrication

Electrical measurements were performed on devices where the CNT tips reach the top surface of the PAA. Metal electrodes were deposited in a Plassys Evaporator at a pressure of 1.00×10^{-7} Torr, with a current of 0.2 A at a deposition rate of 0.3 nm s^{-1}. Four different electrode materials were considered for the deposition: nickel (Ni), aluminum (Al), palladium (Pd) and gold (Au). The thickness of the electrodes was set at 10 nm. A simple shadow mask was mounted on top of the PAA structure. The resulting deposited counter electrodes are squares of approximately 62 500 μm^2.

2.5. Characterization techniques

Scanning electron microscopy (SEM) analyses were performed using a field-emission scanning electron microscope, FE-SEM, HITACHI S4800, with a 5 nm spatial resolution. In order to avoid beam charging effects during analysis, the samples were mounted on a double faced graphite tape. Concerning the TEM observations, a preliminary step consisting of FIB (focused ion beam) lamella preparation was completed [52, 53]. Thus, PAA cross section lamellas were prepared using an FEI-Scios dual beam microscope. Transmission electron microscopy (TEM) and scanning transmission electron microscopy (STEM) analyses were performed on a Jeol 2010F and a Titan-Themis electron microscope, both operating at a 200 kV accelerating voltage. The Titan-Themis is equipped with a Cs probe corrector and a SuperX detector, which allows the chemical analyses of light and heavy elements with a spatial resolution within the picometer range. Chemical mapping was carried out in different areas at the top and bottom pores using the EDX technique.

The crystalline quality of the CNT was checked using a high-resolution confocal Raman microscope (Labram HR800; HORIBA Jobin Yvon, $\lambda = 633$ nm) in the normal incident backscattering configuration.

Electrical measurements were achieved using a Keithley 4200 SCS apparatus using a two-probe system. Such measurements were executed in a closed stainless steel chamber under a N_2 atmosphere.

3. Results and discussion

3.1. Number of branches created by primary pore as a function of the anodization voltage

The exponential voltage decrease process used for thinning the oxide barrier layer at the bottom pores leads to the formation of a branched structure. In the present work, we introduce a novel approach to quantify the number of secondary branches created during the thinning process. The adopted strategy consists of comparing the pore density at the top surface and the pore distribution at the bottom of the pores. Figure 1 shows a schematic representation of the procedure implemented to obtain the number of branches generated by the primary pore (NBPP). After the electrodeposition process, a wet chemical etching step is performed to remove the PAA layer (see figure 1(a)), subsequently, the ratio between the density of pores and nanoparticles can be estimated. Chemical etching is performed in an identical way to the removal of the PAA layer after the first anodization step; this etching process does not impact on the NP distribution because the acidic solution selectively attacks the alumina layer [54]. Such an approach is currently used to remove the PAA template and to expose the previous deposited material [55, 56]. Figure 1(b) highlights a comparison between the pore density (top images) and the density of the deposited nanoparticles (bottom images) giving the procedure and the formula used to calculate the NBPP. Moreover, it can be seen that the pore shape at the bottom of the PAA can be easily estimated by measuring the density of the electrodeposited nanoparticles, which present a higher contrast between the aluminum surface and the deposited nanoparticle, facilitating site counting. If 100% pore filling is achieved, after the deposition process, the nickel nanoparticles completely cover the related 'hole' fingerprint left by the bottom pore. Taking into account that an over-deposition state was avoided, the metal electrodeposition will thus reflect the fingerprint of the previous shape/state of the bottom of the pores. The presented approach is an alternative and faster procedure compared with the direct observation method based on transmission electron microscopy analysis with ion milling [57].

Figure 2 provides information on the calculation of the number of branches generated for each pore. Figure 2(a) plots the density of pores and nanoparticles per unit of area as a function of the anodization voltage. The NP and pore density mean values for each anodization potential were extracted after the counting of the pores and NPs, at ten different spots in the three samples identically prepared. As can be seen, the density of pores decreases as the anodization voltage increases. This is related to the increment of the cell structure size: for a higher anodization potential (as shown in figure S1 of the supplementary material available online at stacks.iop.org/JPMATER/1/015004/mmedia) the pore diameter and interpore distance linearly increase with the applied anodization potential. Concerning the density of the deposited NP, such a value does not significantly vary in the range 20–60 V; this phenomenon is attributed to the similar barrier thinning conditions. From the relation between the density of nanoparticles and the density of the pores, we derived the plot shown in figure 2(b), which estimates the NBPP. As mentioned, when the anodization voltage increases, the number of

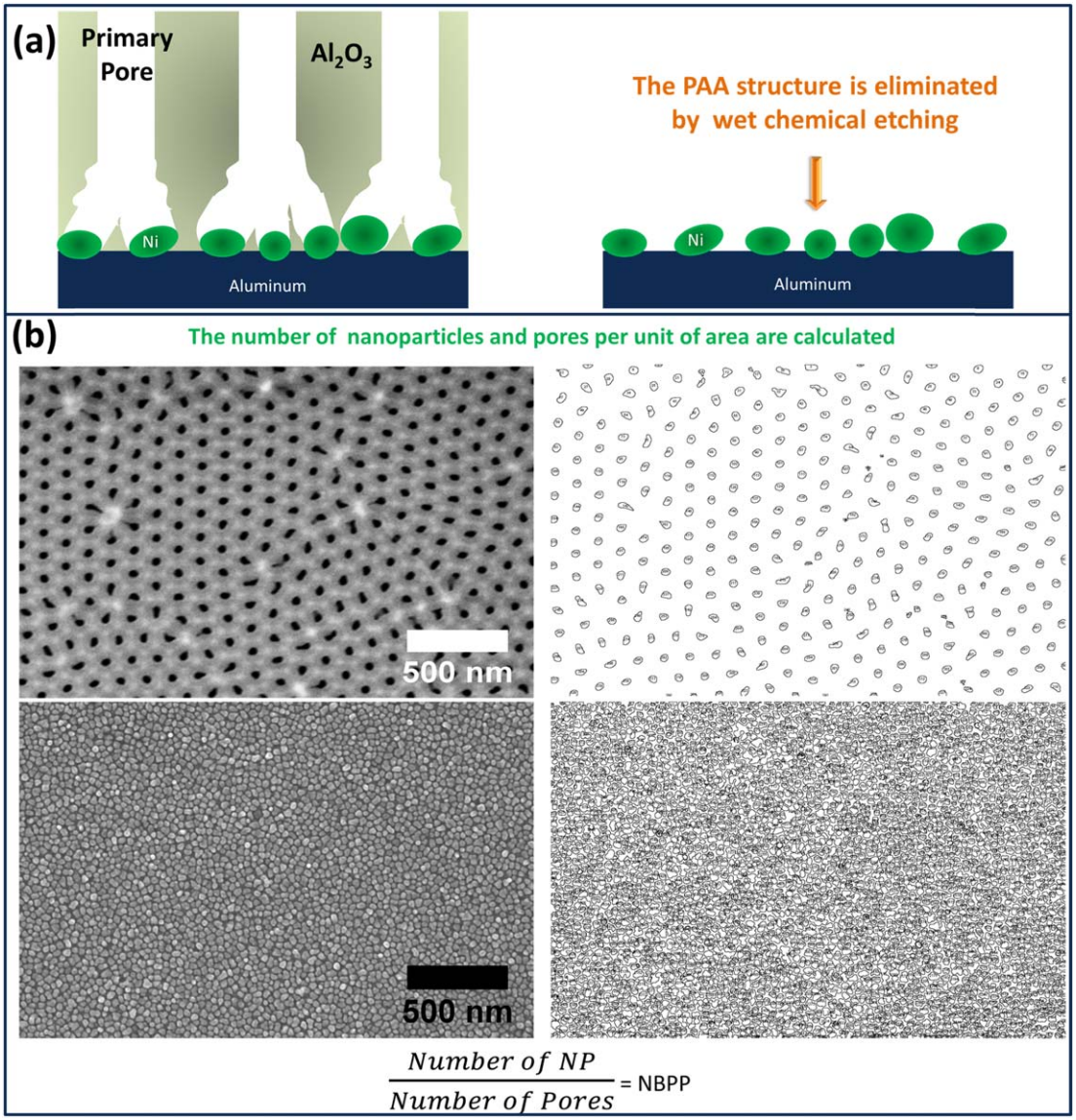

Figure 1. (a) A schematic representation of the formation of secondary branches within the PAA template during the removal of the PAA layer by wet chemical etching, where an electrodeposition process has been performed. (b) A comparison of the pore density (top images) with the density of the deposited nanoparticles (bottom images) and the procedure used to calculate the number of branches generated by the primary pore (NBPP) due to the exponential voltage decrease at the end of the anodization process.

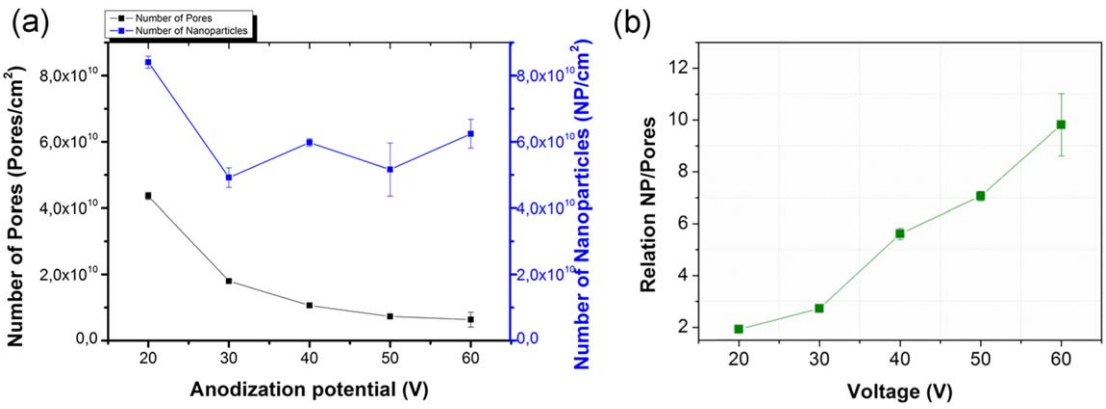

Figure 2. (a) The distribution of the number of pores and NPs per nm^2 as a function of the anodization voltage. (b) The calculated relation between the number of NPs deposited in each pore during the electrodeposition process as a function of the anodization voltage.

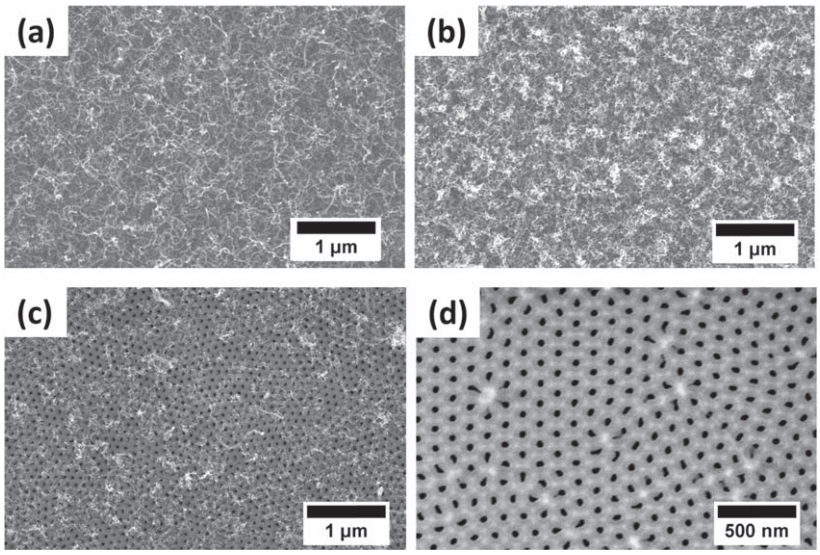

Figure 3. SEM micrographs illustrating the as-synthesized CNTs at the surface of the PAA templates fabricated at different anodization voltages (a) 20 V, (b) 30 V, (c) 40 V and (d) 50 V. The same synthesis conditions were applied for all the samples.

nanoparticles deposited in each pore increases significantly in relative terms. For instance, for an anodization voltage of 20 V, only two nanoparticles are deposited per pore; on the other hand for an anodization voltage of 60 V an average of ten nanoparticles are deposited in each pore. In conclusion, for higher anodization potential, greater branch multiplication is obtained. This phenomenon is related to the fact that the same exponential voltage decrease is imposed regardless of the chosen anodization voltages. As the voltage drops and the final applied voltage is the same in all cases, the boundary conditions for the exponential decrease process imply that the higher anodization voltages will require more time to finalize the thinning process. Consequently, longer exponential voltage decrease processes promote higher branch multiplication.

3.2. Influence of the PAA structure on the synthesis of CNTs within PAA templates

Due to the porous structure, the growth of CNTs inside the PAA is completely different compared with the growth on conventional plane substrates. In the porous configuration, it is more difficult for hydrocarbon species to reach the catalyst nanoparticles. The scenario is aggravated by the presence of a branched structure at the bottom of the pores. Such a structure leads to energy loss in the hydrocarbon molecules due to collisions with the pore walls complicating the carbon precursor's diffusion path towards the catalytic nanoparticle. Representative SEM micrographs of the CNTs grown inside the PAA templates, anodized in the range 20–50 V are presented in figure 3. Aside from the exponential voltage changes, the same conditions were used for the CVD synthesis of all samples. The growth duration was set at 15 min. The SEM analysis indicates that CNT synthesis successfully occurs for anodization voltages of 20 V and 30 V, see figures 3(a) and (b). For both samples, a high and homogeneous CNT distribution is evidenced, presenting a typical spaghetti-like morphology covering the entire PAA template surface. In contrast, when a PAA template is fabricated using a potential of 40 V, the CNT distribution drastically decreases, see figure 3(c). Moreover, when 50 V is used as an anodization voltage it is observed that practically no tubes reach the PAA top surface, as one can see in figure 3(d).

The obtained results are in complete agreement with the previously proposed model, which predicts that a higher branched structure at the bottom of the pores created during the exponential voltage decrease process may significantly hinder the CNT growth. At this stage of analysis, one can conclude that the anodization conditions highly affect the CNT formation. In order to get more insight into the effect imposed by the geometrical features of the PAA templates, TEM analyses were performed on a PAA template fabricated at 40 V. Figure 4 shows cross-section TEM micrographs obtained by lamella preparation, at a low and high magnification of PAA anodized at 40 V and electrodeposited with Ni NP, and finally used for the synthesis of CNT. As can be observed, most of the metal nanoparticles remain in the branched zone, despite the fact that a carbon precursor has been inserted into the reactor for CNT growth. Most of such structures cannot successfully evolve outside the branched pore region. We attributed this phenomenon to the mentioned branched structure at the bottom of the pores that hinders the CNT formation. Figure S2 in the SI, contains TEM micrographs taken at different magnifications on a cross-section lamella, of a branched PAA template containing the catalyst nanoparticles deposited at the bottom pores before initiating the growth.

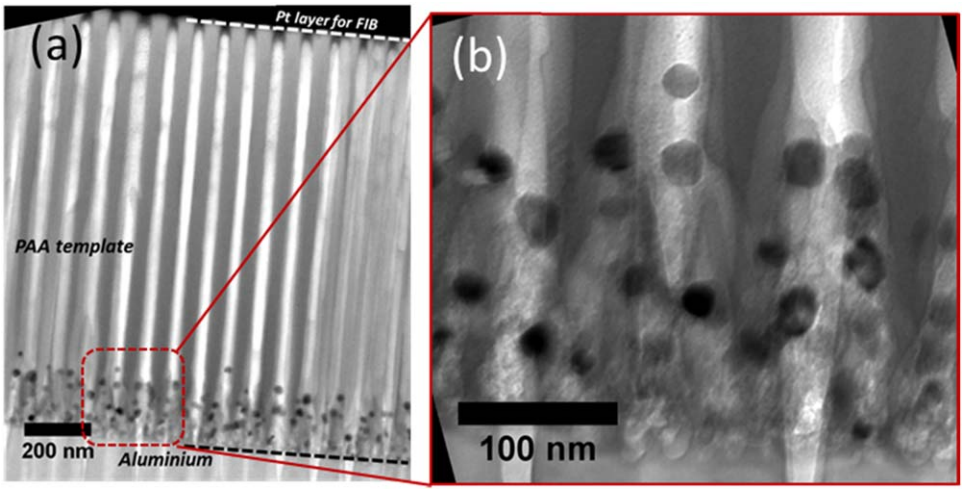

Figure 4. TEM analysis of the FIB cross-section lamella of a PAA template anodized at 40 V, where synthesis of the CNT has been executed: (a) a low magnification TEM image showing the porous structure with the NP located at the branched zone. (b) Zoom on an area of the bottom pores evidencing its branched structure containing the Ni catalyst NP after performing CNT growth.

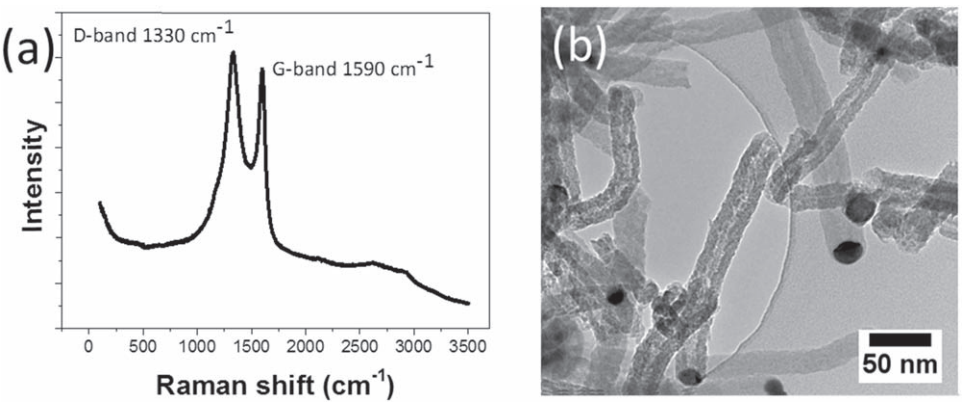

Figure 5. Raman spectra (a) and TEM image (b) of the CNTs grown inside PAA templates anodized at 30 V.

The above-presented results guided us to select voltages in the range 20–30 V for future anodization experiments. As established, the PAA matrix synthesized using these anodization voltages will present rather disordered pore structures [58–60], but they will be able to guarantee the growth of CNTs with higher yields.

3.3. Characteristics of CNTs grown inside PAA templates

To access the morphological and structural information of the synthesized CNTs, Raman spectroscopy and TEM analysis were performed on different samples. No significant differences were observed in the crystallinity of CNTs grown within templates fabricated with anodization voltages in the range of 20–40 V. Figure 5 shows the representative Raman response of carbon nanotubes that have reached the PAA template surface. The spectrum evidences the feature characteristics of CNTs with a strong D-band mode at 1330 cm^{-1} and a G-band mode at 1590 cm^{-1}.

The TEM image represented in figure 5(b) illustrates the morphology of a CNT that has reached the bottom of the PAA templated anodized at 30 V. As can be seen, the tubes present a small diameter varying in the range from 20–40 nm, a characteristic imposed by the PAA templates for which the pore diameter is in the same range. For the analyzed tubes the presence of an irregular channel is related to the defective sidewalls of the tubes, which are characteristic of carbon nanostructures grown at relatively low temperatures.

3.4. CNT growth evolution within PAA templates anodized at 30 V

The dynamic growth evolution of the CNTs inside the PAA templates was investigated, as shown in figure 6. For this purpose, TEM analyses have been performed on FIB cross section lamellas containing the PAA/CNT

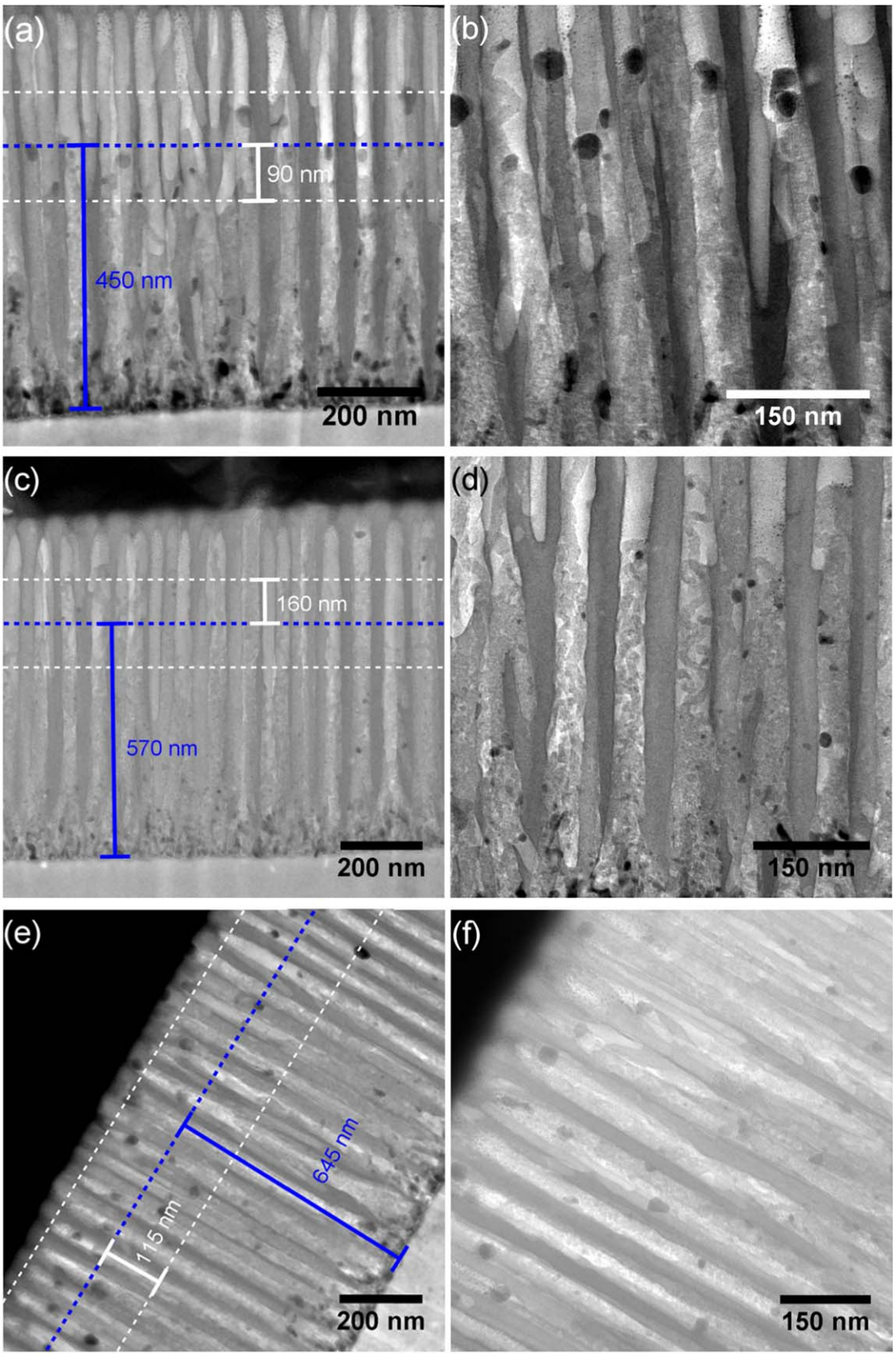

Figure 6. TEM analyses of the FIB cross section lamellas of a PAA/CNT assembly obtained for different growth durations. (a) and (b) 60 s, (c) and (d) 120 s and (e) and (f), 180 s. The CNTs were synthesized using the same PAA templates. The blue dashed lines indicate the average height that the CNT reaches inside the pores. The white dashed lines point out the standard deviation with respect to the mean height value.

assembly at three different growth times. This procedure sheds light on the CNT growth dynamics inside the PAA structure. For instance, figure 6 shows the grown CNT inside the PAA structures interrupted at different times: 60 s for figures 6(a) and (b), 120 s for figures 6(c) and (d), and 180 s for figures 6(e) and (f). We observe that the three prepared samples still contain Ni catalyst at the bottom of the pores. Their presence indicates an excess of deposited catalyst for the carbon nanostructure growth. On the other hand, the PAA/CNT assembly obtained after 180 s highlights that tip-grow mode occurs since there are catalyst-terminated tubes that reach the PAA top surface, as shown in figure S2(c) in the SI. However, it is important to point out that in such cases the diameter of the grown tube is comparable to the pore diameter. When this observation is encountered, only tip-growth mode can occur because the tubes are confined and carbon feedstock can only diffuse through the catalyst. On the other hand and as illustrated in figure 6, some of the Ni catalyst nanoparticles remain at the bottom of the pores. Therefore, a possible base-growth mode mechanism cannot be discarded when the synthesized CNTs are not confined by the pore walls.

A closer analysis of the TEM images for each sample allowed us to determine the average height reached by the CNTs inside the PAA structure as a function of the synthesis duration. The dashed blue lines in figures 6(a), (c) and (e) indicate the mean height that the CNT can reach inside the PAA structure for a different synthesis duration. The white dashed lines indicate the standard deviation of the height reached by the CNT from the mean value. It is important to point out that the height reached by the CNT can highly differ from the CNT length, since more than one CNT can grow in each pore; consequently, the CNTs are not totally confined by the pore walls, as clearly shown in figure 6(d). For example, for a synthesis time of 60 s the CNTs reach an average position of (450 $\pm$ 90) nm from the aluminum side; in this case, no CNT tip was detected on the top surface of the PAA structure (see figure S2(a) in the SI). For a synthesis duration of 120 s, the CNTs achieved an average height of (570 $\pm$ 160) nm. Under such conditions, just a few CNTs can reach the top surface (see figure S4 in SI). When the synthesis takes place for 180 s, the average height reached for the CNT was (645 $\pm$ 110) nm; in this case, one CNT tip reaches the PAA top surface, in 30% of the pores (see figure S3(b) in the SI). The growth rate outside the PAA structure is more complicated to quantify because as already mentioned, without pore wall confinement, as the CNT synthesis evolves with time, the distribution of grown carbon nanostructures leads to a spaghetti-like distribution on the top of the PAA template. Thus it is very difficult to estimate the length of individual CNTs on the PAA surface.

To complete the TEM observation, further chemical analyses using energy dispersive x-ray spectroscopy techniques in the STEM imaging mode of the electron microscope were performed. This type of analysis enables better identification of the CNT and catalyst within the PAA porous structure. As elements of interest, we have chosen the K edges of carbon at 0.27 eV and nickel at 7.47 eV. Figure 7 summarizes the STEM-EDX chemical analyses performed on two different areas, close to the top surface of the PAA porous matrix pores (figures 7(a) and (b)) and close to the bottom surface of the PAA structure (figures 7(c) and (d)), on the sample in which we considered two minutes for tube growth. The poor contrast between the tubes and the PAA in the STEM-HAADF images makes it difficult to identify them inside the pores. In the HAADF-STEM images, the Ni catalyst can be easily identified at the tube tips due to its high atomic number ($Z = 28$). From the STEM-EDX elemental maps, figures 7(b) and (d), obtained for carbon and nickel their exact localization is revealed. Moreover, a closer analysis of the cross section lamella allowed us to observe that for each pore, just one tube arises at the surface of the PAA structure, in agreement with the SEM images in figure S2(b) in the SI section. These results indicate that the tubes that reach the PAA top surface mainly have the same diameter as the host pore. In contrast, we did not observe more than one nanotube tip coming from one pore. This can be attributed to the competition that is expected to take place when more than one tube per pore is nucleated, as evidenced in figure 6(d); entangled CNTs are identified with diameters that are smaller than the pore diameters. This kind of growth highly restricts the tube evolution inside the pore since some of the tubes can be blocked among those trying to emerge from the host pore. Alternatively, if they are not blocked inside the pore, CNTs with a more entangled distribution need more time to reach the PAA top surface since a greater growth length is required, as we can deduce from the set of figures 6 and S2. The competition between the tubes, in this case, is associated with NP morphology. Figure 6(d) shows an area where most of the tubes are entangled and their NP size is smaller than the pore diameter. These kinds of tubes are not observed at the top surface in figures 6(a), (c), and (e); rather tubes with an associated NP size similar to the pore diameter are observed close to the PAA surface as evidenced in figures 6 and S2.

It is generally accepted that the nanotube diameter is mainly determined by the catalyst size. In the present work, we propose that the morphology of the catalyst nanoparticle can determine the carbon nanotube growth behavior inside the vertical-PAA templates. In certain pores, just one carbon nanotube grows with the same diameter as the host pore. However, as confirmed by figure 6, there are pores where more than one tube can nucleate and evolve. In this case, the tubes have a smaller diameter than the host pore. These sets of results evidence that the growth behavior is strongly related to the catalyst nanoparticle morphology at the bottom pores. We proposed a growth mechanism which takes into account the superficial area of the catalyst nanoparticle determined by the host pore. We assume that during the electrodeposition process the same mass

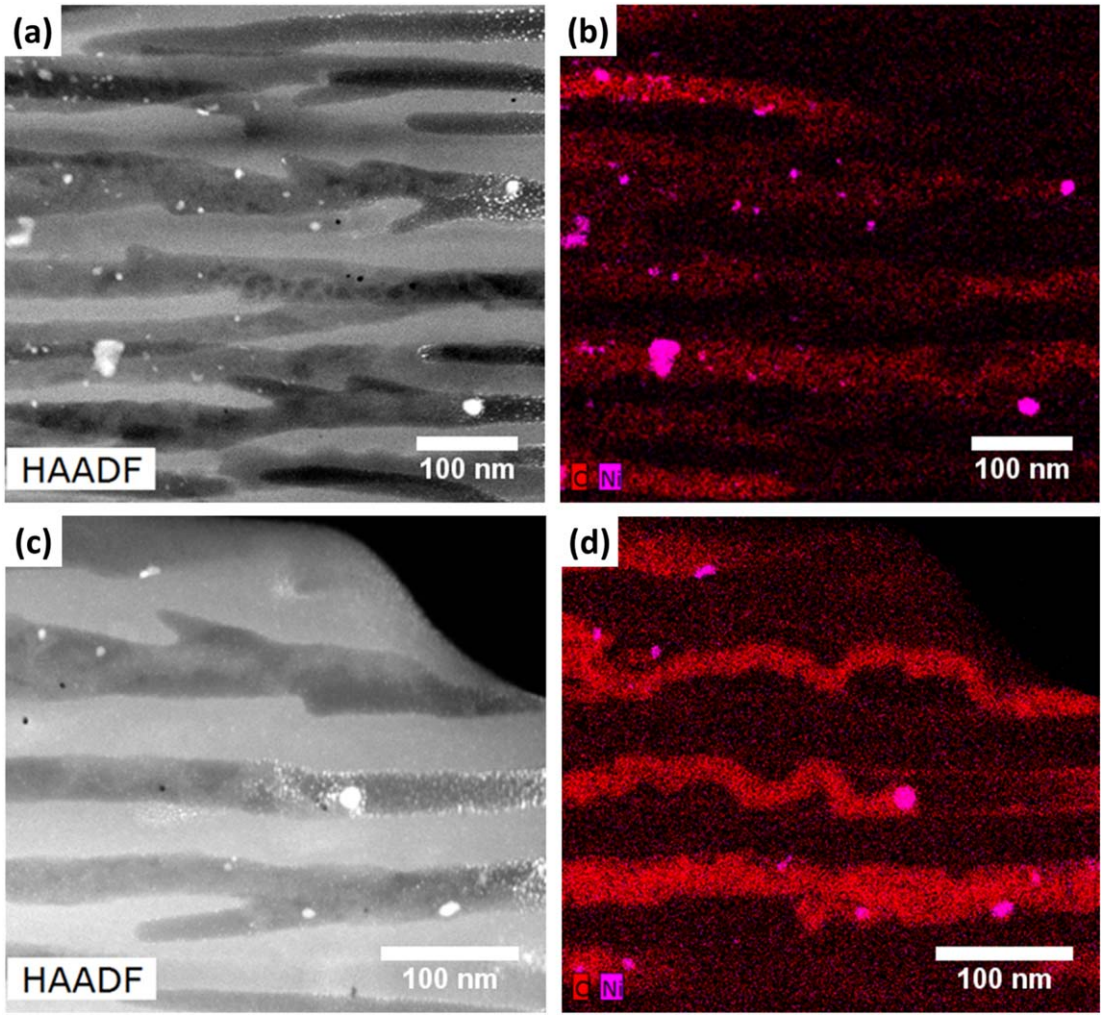

Figure 7. STEM-EDX chemical analysis of two different areas on the sample for which the tube synthesis has been carried out for 120 s. (a) An HAADF-STEM image of the area close to the top of the PAA matrix; (b) the corresponding C/Ni relative map with the carbon represented in red and nickel in pink; (c) an HAADF-STEM image for the area close to the bottom of the PAA matrix; (d) its corresponding C/Ni relative map with the carbon represented in red and nickel in pink.

of catalyst has been deposited in each pore. Basically, when the deposited catalyst nanoparticles do not present a spherical geometry, more than one active site for the CNT synthesis can be created during the pretreatment applied in an H_2 atmosphere. Figure 8 schematizes the proposed growth behavior of the CNT inside the PAA templates depending on the catalyst morphology, which is governed by the bottom pore shape. For the sake of simplicity, in our model, we consider the growth of the CNT without the presence of a nanopore's branched structure, but two different pore shapes, as shown in figure 8(a). After the catalyst electrodeposition, we assume that the catalyst follows the bottom pore shape in both cases (see figure 8(b)). When there is a higher superficial area, after pretreatment in H_2, the catalyst can break/de-wet and more than one catalytic nanoparticle can be formed, as pointed out in figure 8(c). Finally, depending on the nanoparticle morphology, as indicated in figure 8(d), the number of tubes is determined during the synthesis of the CNT. The proposed mechanism takes into account the observations (see figure 6 above) of an excess of the catalyst at the bottom of the pores after the synthesis.

These findings lead us to conclude that the different growth behavior from pore to pore is not only determined by the presence of a branched structure but additionally by the nanoparticle morphology. From the presented results, we presume that the first tubes that arise from the pores are those in which the NP diameter and pore diameter are similar. In this case, no competition is established inside the pore , and the tubes grow as the carbon molecules reach the catalyst. On the other hand, we deduce that there are two reasons why the carbon nanotube cannot emerge from the host pores: (i) the branched structure can block growth when the carbon nanostructures reach the primary pore channel, as shown in figure 4. This growth behavior has been verified for PAA templates fabricated with an anodization voltage of 40 V, where 5.5 branches are created per primary pore. For anodization voltages in the range 20–30 V, between two and three branches per pore are estimated, therefore

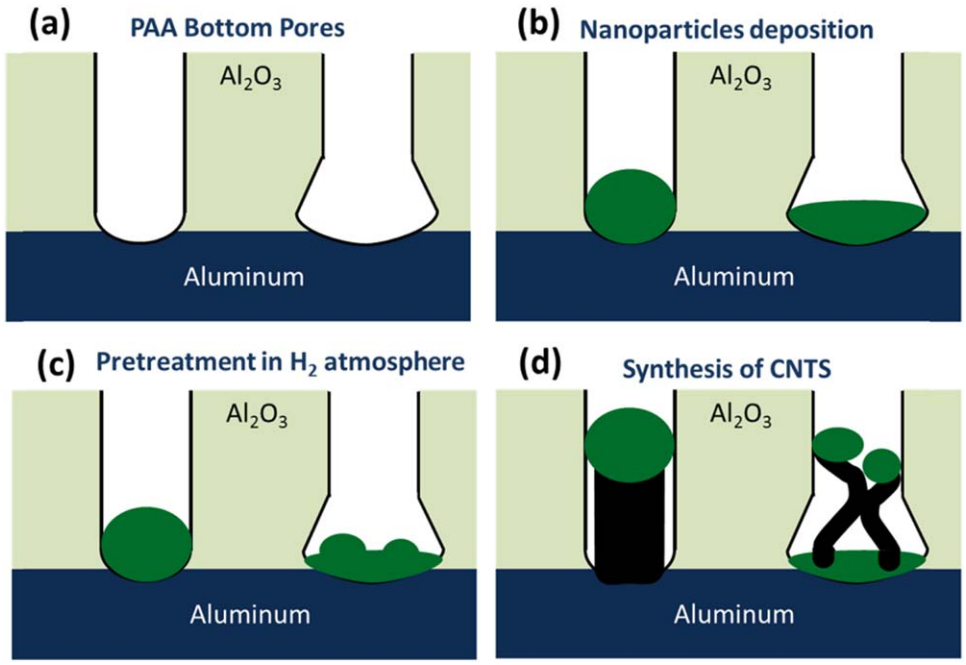

Figure 8. A schematic representation of the proposed growth mechanism used to explain the formation of carbon nanostructures inside the PAA templates. For the sake of simplicity, we considered the growth in a primary pore. (a) The bottom of the pores with different shapes. (b) The catalyst electrodeposited at the bottom of the pores with different morphologies assuming that the same amount of mass has been deposited in each pore. (c) The catalyst morphology after the pretreatment in a H_2 atmosphere. (d) The growth of carbon nanostructures.

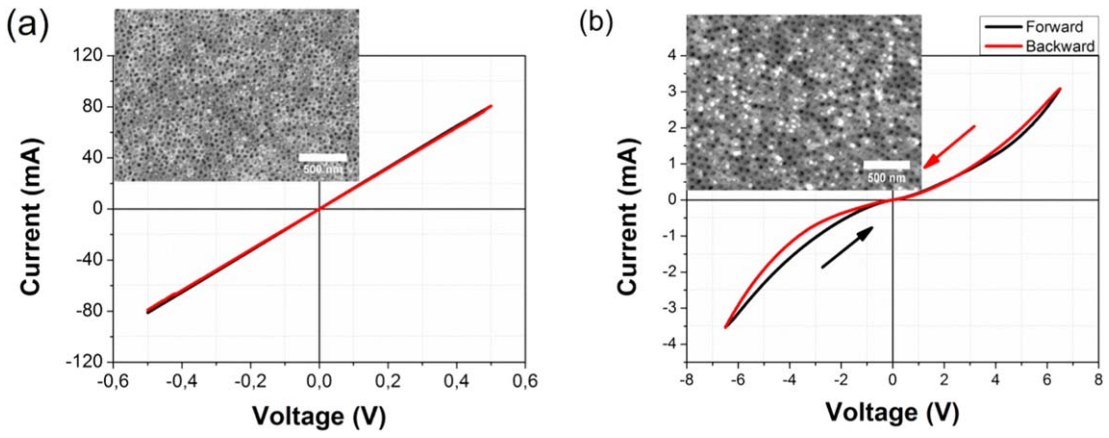

Figure 9. *I–V* curves of devices based on CNTs grown inside PAA templates anodized at different voltages with different CNT density values. Right inset: CNTs emerging from the pores. (a) For the PAA anodized at 20 V, the CNT density emerging from the pores is 2×10^{10} CNT cm^{-2} and (b) for the PAA anodized at 30 V, the density of CNTs emerging from the pores is 6×10^{9} CNT cm^{-2}.

such a phenomenon can also occur (see figure S3 in the SI). (ii) The NP deposited with a high superficial area will induce more than one active site per pore, leading to the competition of numerous tubes with diameters smaller than the pore host diameter, as supported by figure 6(d). However, further studies will have to be performed in order to directly corroborate the influence of the catalyst morphology on the growth of CNTs inside the PAA templates.

3.5. Electrical behavior of devices based on CNTs grown in PAA templates

The electrical behavior of the devices based on CNTs grown in PAA templates was measured after nickel counter electrode deposition on top of the PAA/CNT surface. Figure 9 summarizes the obtained current–voltage (*I–V*) curves for different voltage ranges. Different electrical regimes and corresponding behaviors have been identified depending on the branched structure at the bottom of the pores. For instance, the device anodized at 20 V, as shown in figure 9(a), presents typical resistor-like electrical behavior (see figure S3 to corroborate the

density of CNTs depending on the anodization voltage). In such template fabrication, as a low number of branches are created from the primary pore, the growth of individual tubes in each pore is promoted. We can then consider that the equivalent electrical circuit consists of a CNT connected in parallel between the remaining aluminum and the deposited nickel electrode. On the other hand, when the template is fabricated at 30 V anodization voltage, the number of generated secondary branches are increased and the resulting templates induce a lower density of tubes grown per unit of area, due to the competition between the tubes growing inside the primary pores (see for example the CNT emerging from the PAA shown in figure S2 in the SI). Such a branched structure also induces contact among the tubes inside the pores, which could be correlated to the observed overall increase of the electrical resistance of the device, when the template is anodized at 30 V. Also, the observed nonlinear electrical response for these types of devices can be correlated to the presence of such tube-tube contacts inside the pores. This kind of behavior has previously been reported by Bockrath *et al* [61], providing experimental evidence that the conductance in CNT bundles exhibits Luttinger liquid behavior at low temperatures for the individual CNT [62]. More recently Kozlov *et al* [49] revealed an abnormal zero bias at room temperature in a forest of CNTs. This phenomenon is attributed to the tunneling of the charge carriers across the nanotube junctions, which is enhanced by temperature gradients created by measuring currents and used for the characterization of the nanotube junction network [63]. This phenomenon is consistent with the greater hysteresis effect in the reverse regime since more power is dissipated, which emphasizes the nonlinearities of the device. The nonlinear electron transport in CNT bundles upon exposure to chemical analysis has recently started to be developed as a potential sensing system [60]. To this end, the present fabrication process offers the possibility of obtaining PAA/CNT assemblies with great potential for application in different domains where linear [64] or nonlinear [65] responses are required, by adjusting the number of created branches at the bottom of the pores.

Different metal electrodes have been deposited on the top of the fabricated devices. The electrical behavior is the same for all the top- deposited metals (for further information see figure S5 in SI).

4. Conclusions

The present article explores the growth of CNTs within PAA templates where an exponential voltage decrease process is implemented in order to partially reduce the thickness of the oxide barrier layer at the bottom of the pores. Such a process induces the formation of a branched structure which can determine the density of the subsequently grown CNTs and their growth evolution inside the pores, as well as the electrical behavior of the devices based on such CNTs. The growth dynamics of the CNTs has been analyzed at different time-stages by TEM observations on cross-section FIB lamellas. Such a study provides crucial information on the growth evolution of the tubes and the impact of the PAA structure. We were able to verify that a higher number of branches leads to the competition of the tubes growing inside the primary pores. Such competitive growth conditions inside the pores can even block CNT formation when more than four branches are created. The superficial area of the catalyst is also a geometrical parameter, which can lead to a competitive CNT growth inside the pores. Herein, we propose a model which takes into consideration the shape of the bottom pore. We conclude that under the same electrodeposition conditions, bigger bottom pores promote the electrodeposition of NPs with a bigger surface area, creating more than one nucleating site per pore. The electrical behavior of the devices fabricated from such grown CNT arrays is also determined by the PAA structure at the bottom of the pores. When the number of secondary branches is relatively low, the device behaves as an equivalent resistor formed by parallel connected CNTs between two electrodes. In contrast, the presence of a branched structure induces supplementary tube-tube contacts inside the pores leading to an overall nonlinear response, and an increase of the device's resistance value. Collectively, the presented results provide useful information for establishing a robust process to fabricate devices based on parallel organized CNT arrays, using electrodeposited catalyst nanoparticles inside PAA templates with a tailored bottom pore structure. Additionally, this study provides a novel understanding of the CVD growth evolution of carbon nanostructures inside PAA templates and the impact on the electrical behavior in final devices based on such nanostructures.

Acknowledgments

L S gratefully acknowledges financial support from the Chaire de Recherche PSA AC_3M sponsored by Citroën at the Ecole Polytechnique. This work received support from the French state managed by the National Research Agency under the Investments for the Future program under the reference ANR-10-EQPX-50, TEMPOS-NanoTEM and TEMPOS NanoMax.

ORCID iDs

Leandro Sacco https://orcid.org/0000-0002-5384-2020

References

[1] Balandin A A 2011 Thermal properties of graphene and nanostructured carbon materials *Nat. Mater.* **10** 569
[2] Xie S, Li W, Pan Z, Chang B and Lianfeng S 2000 Mechanical and physical properties on carbon nanotube *J. Phys. Chem. Solids* **61** 1153–8
[3] Cao Q, Han S J, Tulevski G S, Zhu Y, Lu D D and Haensch W 2013 Arrays of single-walled carbon nanotubes with full surface coverage for high-performance electronics *Nat. Nanotechnol.* **8** 180–6
[4] Avouris P, Freitag M and Perebeinos V 2008 Carbon-nanotube photonics and optoelectronics *Nat. Photonics* **2** 341–50
[5] Niyogi S, Hamon M A, Hu H, Zhao B, Bhowmik P, Sen R, Itkis M E and Haddon R C 2002 Chemistry of single-walled carbon nanotubes *Acc. Chem. Res.* **35** 1105–13
[6] Zhang R, Wen Q, Qian W, Su D S, Zhang Q and Wei F 2011 Superstrong ultralong carbon nanotubes for mechanical energy storage *Adv. Mater.* **23** 3387–91
[7] Kanth S K, Sharma A and Park B C 2016 Multiwalled carbon nanotube field emitter as an electron source for a microcolumn *J. Vac. Sci. Technol.* B **34** 11805
[8] Pei T, Zhang P, Zhang Z, Qiu C, Liang S, Yang Y, Wang S and Peng L M 2014 Modularized construction of general integrated circuits on individual carbon nanotubes *Nano Lett.* **14** 3102–9
[9] Felisberto M, Tzounis L, Sacco L, Stamm M, Candal R, Rubiolo G H and Goyanes S 2017 Carbon nanotubes grown on carbon fiber yarns by a low temperature CVD method: a significant enhancement of the interfacial adhesion between carbon fiber/epoxy matrix hierarchical composites *Compos. Commun.* **3** 33–7
[10] De Volder M F L, Tawfick S H, Baughman R H and Hart A J 2013 Carbon nanotubes: present and future commercial applications *Science* **339** 535–9
[11] Florea I, Ersen O, Arenal R, Ihiawakrim D, Messaoudi C, Chizari K, Janowska I and Pham-Huu C 2012 3D analysis of the morphology and spatial distribution of nitrogen in nitrogen-doped carbon nanotubes by energy-filtered transmission electron microscopy tomography *J. Am. Chem. Soc.* **134** 9672–80
[12] Chizari K, Janowska I, Houllé M, Florea I, Ersen O, Romero T, Bernhardt P, Ledoux M J and Pham-Huu C 2010 Tuning of nitrogen-doped carbon nanotubes as catalyst support for liquid-phase reaction *Appl. Catal. A Gen.* **380** 72–80
[13] Li A P, Müller F, Birner A, Nielsch K and Gösele U 1998 Hexagonal pore arrays with a 50–420 nm interpore distance formed by self-organization in anodic alumina *J. Appl. Phys.* **84** 6023–6
[14] Zaraska L, Sulka G D and Jaskula M 2011 Anodic alumina membranes with defined pore diameters and thicknesses obtained by adjusting the anodizing duration and pore opening/widening time *J. Solid State Electrochem.* **15** 2427–36
[15] Alsawat M, Altalhi T, Kumeria T, Santos A and Losic D 2015 Carbon nanotube-nanoporous anodic alumina composite membranes with controllable inner diameters and surface chemistry: influence on molecular transport and chemical selectivity *Carbon N. Y.* **93** 681–92
[16] Sklar G P, Paramguru K, Misra M and LaCombe J C 2005 Pulsed electrodeposition into AAO templates for CVD growth of carbon nanotube arrays *Nanotechnology* **16** 1265–71
[17] Kim K H, Brunel D, Gohier A, Sacco L, Châtelet M and Cojocaru C S 2014 Cup-stacked carbon nanotube Schottky diodes for photovoltaics and photodetectors *Adv. Mater.* **26** 4363–9
[18] Masuda H and Fukuda K 1995 Ordered metal nanohole arrays made by a two-step replication of honeycomb structures of anodic alumina *Science* **268** 1466–8
[19] Xu D, Chen D, Xu Y, Shi X, Guo G, Gui L and Tang Y 2000 Preparation of II–VI group semiconductor nanowire arrays by dc electrochemical deposition in porous aluminum oxide templates *Pure Appl. Chem.* **72** 127–35
[20] Zafar N, Shamaila S, Sharif R, Wali H, Naseem S, Riaz S and Khaleeq-Ur-Rahman M 2015 Effects of pH on the crystallographic structure and magnetic properties of electrodeposited cobalt nanowires *J. Magn. Magn. Mater.* **377** 215–9
[21] Ba L and Li W S 2000 Influence of anodizing conditions on the ordered pore formation in anodic alumina *J. Phys. D: Appl. Phys.* **33** 2527–31
[22] Liang J, Chik H, Yin A and Xu J 2002 Two-dimensional lateral superlattices of nanostructures: nonlithographic formation by anodic membrane template *J. Appl. Phys.* **91** 2544–6
[23] Furneaux R C, Rigby W R and Davidson A P 1989 The formation of controlled-porosity membranes from anodically oxidized aluminium *Nature* **337** 147–9
[24] Marquardt B, Eude L, Gowtham M, Cho G, Jeong H J, Châtelet M, Cojocaru C S, Kim B S and Pribat D 2008 Density control of electrodeposited Ni nanoparticles/nanowires inside porous anodic alumina templates by an exponential anodization voltage decrease *Nanotechnology* **19** 405607
[25] Sui Y C, González-León J A, Bermúdez A and Saniger J M 2001 Synthesis of multi branched carbon nanotubes in porous anodic aluminum oxide template *Carbon N. Y.* **39** 1709–15
[26] Angelucci A, Ciorba A, Malferrari L, Odorici F, Rizzoli R, Rossi M, Sessa V, Terranova M L and Veronese G P 2009 Field emission properties of carbon nanotube arrays grown in porous anodic alumina *Phys. Status Solidi* **6** 2164–9
[27] Lee J S, Gu G H, Kim H, Jeong K S, Bae J and Suh J S 2001 Growth of carbon nanotubes on anodic aluminum oxide templates: Fabrication of a tube-in-tube and linearly joined tube *Chem. Mater.* **13** 2387–91
[28] Jeong B, Uhm S, Kim J H and Lee J 2013 Pyrolytic carbon infiltrated nanoporous alumina reducing contact resistance of aluminum/carbon interface *Electrochim. Acta* **89** 173–9
[29] Watts P C P, Mureau N, Tang Z, Miyajima Y, David Carey J and Silva S R P 2007 The importance of oxygen-containing defects on carbon nanotubes for the detection of polar and non-polar vapours through hydrogen bond formation *Nanotechnology* **18** 175701
[30] Kim M J, Choi J H, Park J B, Kim S K, Yoo J B and Park C Y 2003 Growth characteristics of carbon nanotubes via aluminum nanopore template on Si substrate using PECVD *Thin Solid Films* **435** 312–7
[31] Ciambelli P, Sannino D, Sarno M, Fonseca A and Nagy J B 2004 Hydrocarbon decomposition in alumina membrane: an effective way to produce carbon nanotubes bundles *J. Nanosci. Nanotechnol.* **4** 779–87
[32] Golshadi M, Maita J, Lanza D, Zeiger M, Presser V and Schrlau M G 2014 Effects of synthesis parameters on carbon nanotubes manufactured by template-based chemical vapor deposition *Carbon N. Y.* **80** 28–39

[33] Ciambelli P, Arurault L, Sarno M, Fontorbes S, Leone C, Datas L, Sannino D, Lenormand P and Du Plouy S L B 2011 Controlled growth of CNT in mesoporous AAO through optimized conditions for membrane preparation and CVD operation *Nanotechnology* **22** 265613
[34] Sui Y C, Acosta D R, González-León J A, Bermúdez A, Feuchtwanger J, Cui B Z, Flores J O and Saniger J M 2001 Structure, thermal stability, and deformation of multibranched carbon nanotubes synthesized by CVD in the AAO template *J. Phys. Chem.* B **105** 1523–7
[35] Haase M R, Alvarez N T, Malik R, Schulz M and Shanov V 2015 Unifying the templating effects of porous anodic alumina on metallic nanoparticles for carbon nanotube synthesis *J. Nanoparticle Res.* **17** 359
[36] Jeong S-H, Hwang H-Y, Hwang S-K and Lee K-H 2004 Carbon nanotubes based on anodic aluminum oxide nano-template *Carbon N. Y* **42** 2073–80
[37] Maschmann M R, Franklin A D, Amama P B, Zakharov D N, Stach E A, Sands T D and Fisher T S 2006 Vertical single- and double-walled carbon nanotubes grown from modified porous anodic alumina templates *Nanotechnology* **17** 3925–9
[38] Sayer R A, Engerer J D, Vidhyadhiraja N S and Fisher T S 2013 Length and temperature dependent 1/f noise in vertical single-walled carbon nanotube arrays *J. Appl. Phys.* **113** 144306
[39] Ke N J, Downard A J and Golovko V B 2015 Carbon nanotube diameter control via catalytic Co nanoparticles electrodeposited in porous alumina membranes *RSC Adv.* **5** 25747–54
[40] Rana K, Kucukayan-Dogu G and Bengu E 2012 Growth of vertically aligned carbon nanotubes over self-ordered nano-porous alumina films and their surface properties *Appl. Surf. Sci.* **258** 7112–7
[41] Jeong S H, Lee O J, Lee K H, Oh S H and Park C G 2002 Preparation of aligned carbon nanotubes with prescribed dimensions: Template synthesis and sonication cutting approach *Chem. Mater.* **14** 1859–62
[42] Kim K H, Gohier A, Bourée J E, Châtelet M and Cojocaru C S 2015 The role of catalytic nanoparticle pretreatment on the growth of vertically aligned carbon nanotubes by hot-filament chemical vapor deposition *Thin Solid Films* **575** 84–91
[43] Bayle-Guillemaud P, Radtke G and Sennour M 2003 Electron spectroscopy imaging to study ELNES at a nanoscale *J. Microsc.* **210** 66–73
[44] Grogger W, Hofer F, Kothleitner G and Schaffer B 2008 An introduction to high-resolution EELS in transmission electron microscopy *Top. Catal.* **50** 200–7
[45] Yang M H, Teo K B K, Milne W I and Hasko D G 2005 Carbon nanotube Schottky diode and directionally dependent field-effect transistor using asymmetrical contacts *Appl. Phys. Lett.* **87** 1–3
[46] Chen Z, Appenzeller J, Knoch J, Lin Y and Avouris P 2005 The role of metal/nanotube contact in the performance of carbon nanotube field-effect transistors *Nano Lett.* **5** 1497–502
[47] Berger C, Yi Y, Wang Z L and Heer W A D 2002 Multiwalled carbon nanotubes are ballistic conductors at room temperature *Appl. Phys. A Mater. Sci. Process* **74** 363–5
[48] Rochford C, Limmer S J, Howell S W, Beechem T E and Siegal M P 2014 Planarized arrays of aligned, untangled multiwall carbon nanotubes with Ohmic back contacts *J. Mater. Res.* **30** 315–22
[49] Kozlov M E 2011 Nonlinear electrical properties of carbon nanotube forests *Appl. Phys. Lett.* **99** 133111
[50] Xu Y F, Liu H, Li X J, Kang W M, Cheng B W and Li X J 2015 A novel method for fabricating self-ordered porous anodic alumina with wide interpore distance using phosphoric/oxalic acid mixed electrolyte *Mater. Lett.* **151** 79–81
[51] Sacco L, Florea I, Châtelet M and Cojocaru C-S 2018 Investigation of porous anodic alumina templates formed by anodization of single-crystal aluminum substrates *Thin Solid Films* **660** 213–20
[52] Giannuzzi L A and Stevie F A 1999 A review of focused ion beam milling techniques for TEM specimen preparation *Micron* **30** 197–204
[53] Bassim N D, De Gregorio B T, Kilcoyne A L D, Scott K, Chou T, Wirick S, Cody G and Stroud R M 2012 Minimizing damage during FIB sample preparation of soft materials *J. Microsc.* **245** 288–301
[54] Zhou J H, He J P, Zhao G W, Zhang C X, Zhao J S and Hu H P 2007 Alumina nanostructures prepared by two-step anodization process *Trans. Nonferrous Met. Soc. China* English Ed. **17** 82–6
[55] Zhang X Y, Zhang L D, Chen W, Meng G W, Zheng M J, Zhao L X and Phillipp F 2001 Electrochemical fabrication of highly ordered semiconductor and metallic nanowire arrays *Chem. Mater.* **13** 2511–5
[56] Zaraska L, Sulka G D and Jaskuła M 2010 Porous anodic alumina membranes formed by anodization of AA1050 alloy as templates for fabrication of metallic nanowire arrays *Surf. Coatings Technol.* **205** 2432–7
[57] Lee S, Kim D, Gillette E, Oh J, Han S W and Lee S B 2013 Anodized pore structural evolution of focused ion beam patterned Al: direct analysis of branched nanopores and nanosacks *Phys. Chem. Chem. Phys.* **15** 10659
[58] Nielsch K, Choi J, Schwirn K, Wehrspohn R B and Gösele U 2002 Self-ordering regimes of porous alumina: the 10 porosity rule *Nano Lett.* **2** 677–80
[59] Sulka G D and Stepniowski W J 2009 Structural features of self-organized nanopore arrays formed by anodization of aluminum in oxalic acid at relatively high temperatures *Electrochim. Acta* **54** 3683–91
[60] Kashi M A and Ramazani A 2005 The effect of temperature and concentration on the self-organized pore formation in anodic alumina *J. Phys. D: Appl. Phys.* **38** 2396–9
[61] Bockrath M W, Cobden D H, Lu J, Rinzler A G, Smalley R E, Balents L and McEuen P L 1999 Luttinger-liquid behaviour in carbon nanotubes *Nature* **397** 598–601
[62] Jang W Y, Kulkarni N N, Shih C K and Yao Z 2004 Electrical characterization of individual carbon nanotubes grown in nanoporous anodic alumina templates *Appl. Phys. Lett.* **84** 1177–9
[63] Nakanishi T and Ando T 2001 Electrical transport through crossed carbon nanotube junctions *AIP Conf. Proc.* pp 149–52
[64] Jiang D, Mu W, Chen S, Fu Y, Jeppson K and Liu J 2015 Vertically stacked carbon nanotube-based interconnects for through silicon via application *IEEE Electron. Device Lett.* **36** 499–501
[65] Gowda P, Suri A, Reddy S K and Misra A 2014 Chemical vapor detection using nonlinear electrical properties of carbon nanotube bundles *Nanotechnology* **25** 025708